



Toward Efficient Cold Spraying of Inconel 718: Understanding the Influence of Coating and Particle Impact Temperatures

Roberto Ortiz-Fernandez¹ · Bertrand Jodoin²

Submitted: 3 May 2022 / in revised form: 18 October 2022 / Accepted: 23 October 2022 / Published online: 15 November 2022
© ASM International 2022

Abstract The production of Inconel 718 coatings using the cold spray process is often challenging due to the limited plastic deformation of particles upon impact associated with its mechanical properties. This leads to the requirement of high spray parameters to achieve dense coating build-up that may result in high and complex residual stresses that can also affect negatively the substrate and lead to nozzle clogging. In this work, the role of the coating and particle impact temperatures is investigated while ensuring they are decoupled from the particle impact velocity. This allows starting to explore potential ways to produce a sound and quality Inconel 718 coating at reduced spray parameters. To decouple and evaluate the role of the particle impact temperature, powder preheating units with downstream injection are used to decouple the particle impact temperature from the particle impact velocity. Three initial particle temperatures are studied: 25, 400 and 750 °C. The effect of the coating temperature on the deposition process is investigated by controlling this temperature independently of the gas stagnation temperature through the use of induction heating. Deposition efficiency, porosity, and micro-hardness are used to assess the coating quality. The coating time–temperature history is measured to better understand its influence on the deposition of Inconel 718. In this work, an enhanced understanding of the effect of both particle and coating temperatures on the

coating process is obtained, and the findings allow the establishment of a potential approach to produce dense coatings using reduced spray parameters.

Keywords coating temperature · cold spray · feedstock · inconel · particle temperature · processing · Ti-6Al-4 V

Introduction

Inconel 718 (In718) is a nickel-based superalloy characterized by its excellent mechanical properties from cryogenic temperatures up to 650 °C (Ref 1–4). It also exhibits excellent performance in high corrosion environments, and is resistant to oxidation at elevated temperatures (Ref 2–4). These characteristics have made In718 a coating material of interest in the power generation and aerospace fields. Deposition of In718 coatings has been achieved using thermal spray processes such as high-velocity oxygen fuel (HVOF) (Ref 5–7) and atmospheric plasma spraying (APS) (Ref 8, 9). However, coatings produced by these techniques are usually characterized by a high level of oxide inclusions and porosities (Ref 5–7, 9). Additionally, the associated powder melting/solidification leads to undesirable phase transformations (Ref 5–9).

Cold Spray (CS) has emerged as an alternative method for the production of In718 coatings (Ref 9–26). In CS, feedstock powder particles are injected into a converging/diverging nozzle and accelerated to high velocities by a supersonic gas flow prior to impacting and deforming onto the substrate (Ref 27, 28). During the solid-state deformation of the particles occurring at high strain rates, approximately 90% their kinetic energy is converted into heat while the remaining is transformed into elastic and plastic deformation (Ref 28). Particles bond to the substrate

✉ Roberto Ortiz-Fernandez
rorti045@uottawa.ca

¹ Cold Spray Laboratory, University of Ottawa, 161 Louis Pasteur Room A205B Pavilion Colonel By, Ottawa, ON K1N 6N5, Canada

² Faculty of Engineering, University of Ottawa, 770 King Edward Avenue, Ottawa, ON K1N 6N5, Canada

if intimate oxide-free contacts are created at the interfaces allowing metallic bonds and by mechanically anchoring to the substrate (Ref 29, 30).

It has been found that the exceptional mechanical properties of In718 hinder the production of dense CS In718 coatings by limiting plastic deformation upon impact (Ref 10, 13, 26). As such, production of CS In718 coatings have required using a high operating gas pressure (up to 5 MPa) and temperature (up to 1000 °C) (Ref 9–26). With these spray parameters, η (the non-dimensional ratio of $V_{\text{impact}}/V_{\text{critical}}$) values ranging from 1.09 to 1.43 have been reported for the production of In718 coatings (Ref 10–12). High operating gas temperatures increase the gas velocity, while high operating gas pressures increase the gas density, both leading to enhanced particle impact velocity (Ref 31–33). Additionally, by feeding the powder into an elongated pre-chamber or converging region of the nozzle, an increase in the particle impact temperature is achieved as a result of the heat transfer with the hot slow gas (Ref 34, 35). Higher particle impact temperatures promote thermal softening facilitating plastic deformation upon their impact (Ref 35–37). The combination of relatively high particle velocities and temperatures for the deposition of In718 coatings has shown promising results, but porous coatings ($\geq 1.5\%$) are still observed (Ref 10–12, 14, 16, 19–22, 26). Furthermore, nozzle clogging near the throat area has been reported when operating at high gas temperatures (Ref 10, 14, 16, 19) and substrate damage (bending) has been observed as a result of the high temperatures recovered at the substrate surface (stagnation) while spraying (Ref 9, 16).

A potential alternative to avoid these issues resulting from using high operating gas temperatures is the use of reduced spray parameters. This approach has never been explored for the production of In718 coatings because studies have demonstrated that increasing the operating gas temperatures often leads to higher deposition efficiency values and a less porous coating due to the higher particle impact velocities and temperatures (Ref 10, 19, 26). However, other studies have demonstrated that this is not always the case as higher DE values and more porous coatings have also been reported for materials such as aluminum, MCrAlY, and Al-12Si (Ref 38–40). These contradictory results demonstrate that the influence of the particle impact temperature on the overall coating quality (DE and coating porosity values) has not yet been completely understood.

Few studies have been devoted to assess the role of the coating temperature on the CS deposition process (Ref 41–47) as maintaining a constant coating temperature becomes difficult due to heat exchanged with the impacting propellant gas (Ref 46, 47). In previous studies, the coating temperature has been raised using a laser system coupled to

the CS process. In the laser-assisted CS process, increasing the coating temperature is mostly limited to the spot size of the laser which creates a very localized and instantaneous raise in temperature (Ref 41–45). A detailed and validated model has shown that, for the copper-on-steel combination, the effect of the laser spot is limited to up to 3 mm in coating thickness, and the local coating heating lasts less than 5 s (Ref 48). Recently, the induction heating (IH) and CS processes were coupled (IHCS) to allow a more uniform coating heating in the case of pure Aluminum (Ref 46, 47). However, the effect of the coating temperature on the deposition of In718 has not yet been reported.

The objective of the current study is to investigate the effect of both particle impact and coating temperatures on the deposition of In718 and explore the effect of using reduced spray parameters that could minimize the possibilities of nozzle clogging, deformed substrate due to high temperature and high residual stresses. The influence of particle impact velocity on the production of In718 coatings is also investigated. To properly characterize the effect of the particle temperature, this variable is decoupled from the gas stagnation temperature (and therefore particle impact velocity) by using controlled powder preheating. Additionally, the powder is fed in the diverging section of the nozzle to prevent heat exchange between the powder and the hot slow propellant gas that is otherwise unavoidable and impossible to control. Three initial particle temperatures (leading to three different particle impact temperatures) are evaluated: 25, 400, and 750 °C. The particle impact temperature and velocity are predicted using a validated three-dimensional computational fluid dynamics (CFD) model. The CS process is assisted by an IH system to investigate the role of the coating temperature on the production of In718 coatings and the coating time–temperature history is measured for the two initial temperatures: 25 and 600 °C. DE, coating porosity level, coating micro-hardness and thickness are evaluated to characterize the influence of the coating and particle impact temperatures on the CS deposition of In718 coatings.

Experimental Procedures

Feedstock and Substrate Materials

Commercially available gas-atomized In718 powder (TrueFrom718, Praxair Surface Technologies, Indianapolis, IN, USA) was used as the feedstock material. This powder is characterized by a spherical shape and smooth surface, as shown in Fig. 1. The chemical composition (weight percentage) is Ni-19Cr-18Fe-Nb-5Ta-3Mo-1Ti. The powder particle size ranges between 10 and

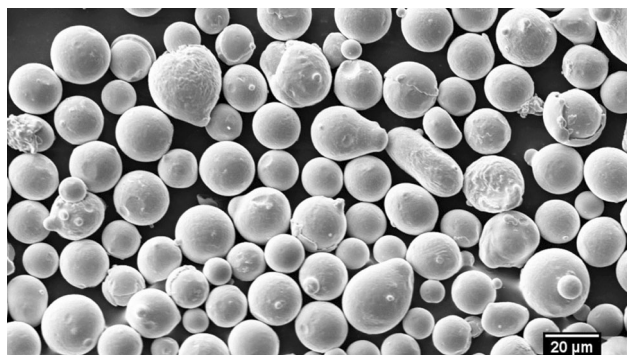


Fig. 1 Scanning electron microscope images of the In718 feedstock power

45 μm , with an average particle size of approximately 30 μm , according to the manufacturer's data sheet.

The substrate material was commercially available Ti-6Al-4 V (Ti64) alloy bars of 25.4 mm in diameter (Titanium Industries, Inc., Montreal, QC, Canada). The bars were sectioned into 45 mm thick coupons. This substrate material was chosen because previous studies focused on evaluating the role of the substrate and coating temperatures on the CS process have used this substrate material removing one variable to consider when assessing the results (Ref 46, 47, 49). Additionally, Ti64 also provides further understanding of the influence of the coating temperature on the deposition of the hard-on-hard (In17-on-Ti64) material combination. The manufacturer's data sheet indicated a composition by weight percentage of Ti – balance, Al – 5.94, V – 4%. The coupons were ground with water as a lubricant prior to being coated. The resulting arithmetic average roughness (RA) after the grinding process was $0.45 \pm 0.07 \mu\text{m}$, measured using a profilometer equipped with a diamond stylus (Phase II, SRG-4000, NJ, USA). The substrates were cleaned and degreased in an ethanol ultrasonic bath for 3 min prior to the start of the deposition process.

Consolidation Parameters

A commercially available CS system (SST-EPX, Centerline (Windsor) Limited, Windsor, ON, Canada) was used. This type of equipment was chosen because it allows controlling the particle temperature at the diverging section of the nozzle independently from the operating gas temperature, as the powder is fed downstream. To increase the initial particle temperature at the injection location, two powder-preheating units were used. A commercially available powder preheating unit (Centerline (Windsor) Limited, Windsor, ON, Canada) was used to increase the initial particle temperature to 400 $^{\circ}\text{C}$ prior to being fed into the nozzle diverging section. This commercial powder

preheating unit is designed to increase the initial particle temperature to a maximum of 500 $^{\circ}\text{C}$ within the coil length. The powder-preheating unit consisted of a stainless steel coiled tube, and its temperature is increased by a heater radiating onto the coiled tube surface. The powder-preheating unit included two built-in thermocouples, one at the inlet and the other at the outlet of the coiled tube, to control the tube wall temperature. The unit was assumed to reach a steady-state temperature when the wall temperature difference between the inlet and outlet was less than 2 $^{\circ}\text{C}$. Due to the extensive length of the heating tube, it is assumed that by the time the gas and the particles exited the powder-preheating unit, these had reached the tube wall temperature.

To increase the initial particle temperature above 500 $^{\circ}\text{C}$, an in-house powder preheater unit is used. This preheating unit consists of a mixing T and a stainless steel coil in which a heated gas and a cold gas with powder are brought together to reach a mixed gas temperature (T_{mixed}). The coil is perfectly insulated from the exterior to avoid any potential heat loss to the environment. The coil was designed to ensure equilibrium between the gas and the powder particles at a temperature equal to T_{mixed} by the time the powder exits the coil (Ref 50). The coil is close to 5 m in length, and a schematic of the in-house powder preheating unit is presented in Fig. 2.

A WC–Co nozzle (Utilife, Centerline (Windsor) Limited, Windsor, ON, Canada) with a throat and exit diameters of 2 and 6.3 mm, respectively, was used. The nozzle diverging section has a 120 mm length. Table 1 presents the CS parameters used for the production of the samples, which are the maximum gas stagnation conditions that the system can reach.

The IHCS system consisted of an induction heating system (Tucker Induction Sys. Inc., Shelby Township, MI, USA) coupled to the SST-EPX equipment (Ref 46, 47). The copper planar round coil had an outer and inner diameter of 110.0 mm and 42.0 mm, respectively, as presented in Fig. 3(b). The coil had a total of four turns. The inner and outer diameters of the coil tubing were 5.0 and 6.3 mm, respectively. The substrates were positioned in the center of the IH coil, as presented in Fig. 3. The IH was kept “On” before and during the spraying process when IHCS was used. For the IHCS process, the initial substrate surface temperature was 600 $^{\circ}\text{C}$, as a result of the eddy currents quickly heating up the substrate prior to the start of the spraying process. The IH parameters were 68 A and 193 kHz which are the highest IH parameters the system can reach for this specific substrate-coating configuration. For the cases in which the IH system was not coupled to the CS process, the initial substrate temperature was 25 $^{\circ}\text{C}$. 25 and 600 $^{\circ}\text{C}$ as the initial substrate temperatures were selected for consistency purposes based on previous

Fig. 2 Schematic of the In-house powder preheater. Hot (T_{hot}) and cold (T_{cold}) gases are brought together and mixed inside a stainless steel coil. Powder is fed into the coil with the cold gas

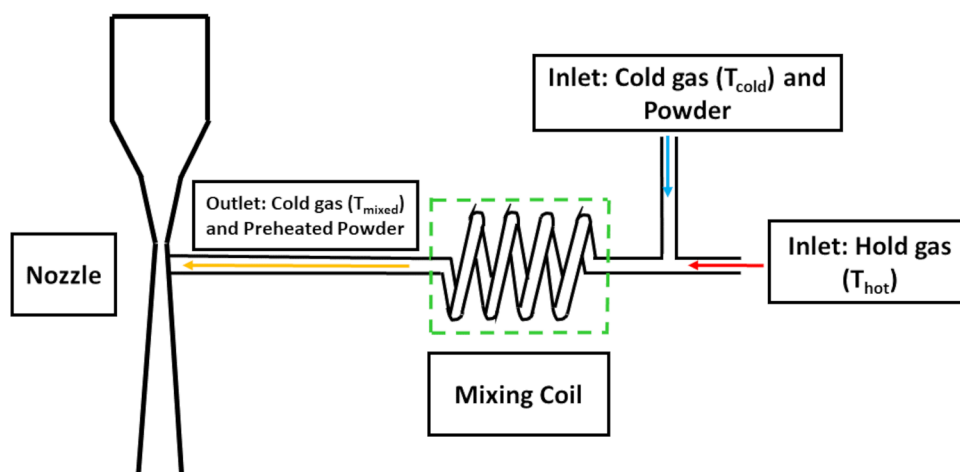


Table 1 Cold Spray deposition parameters

General deposition parameters	Values	
Propellant Gas	Nitrogen	Helium
Stagnation Temperature (T_0) (°C)	500	500
Stagnation Pressure (P_0) (MPa)	3.45	2.06
Initial Powder Temperature (°C)	25, 400, and 750	
Traverse Speed (mm/s)	120	
Powder Feed rate (g/s)	1	
Stand-off distance (SOD) (mm)	15	
Number of passes	5	
Step Size (mm)	1	

investigations of the influence of the substrate temperature on the CS deposition for the deposition of aluminum-on-Ti64 substrates (Ref 46, 47, 49).

To monitor the coating time–temperature history, a Ti64 substrate was first coated with a single-layer In718 coating using nitrogen as the propellant gas (500 °C and 3.45 MPa). Once the sample was prepared, it was set aside to let it cool down to room temperature before trials were performed using that pre-coated sample. Because the single-layer coating was thin ($\leq 30 \mu\text{m}$), it was assumed that during the deposition of this layer, the coating reached the initial substrate temperature. For that reason, as a first approximation, 25 and 600 °C were used as the initial coating temperature. The coating surface time–temperature history was monitored using two non-contact infrared thermometers. A RAYGPRSF (Raytek, Santa Cruz, CA, USA) non-contact infrared thermometer was used to measure the coating surface time–temperature history when the initial coating temperature was 25 °C. This infrared thermometer has a maximum working range of approximately 540 °C. For that reason, a second non-contact infrared thermometer was needed. The OptCT3MH2SF (Optris, Portsmouth, NW,

USA) was used to measure the coating time–temperature history when the initial coating temperature was 600 °C. The OptCT3MH2SF has a working range of 200 up to 1500 °C. The infrared thermometers monitored the coating temperature-history 7.5 mm away from the middle of the bar top surface, as shown in Fig. 3(b).

Table 2 presents a summary of the samples produced in this work using different combinations of production methods and initial particle and coating temperatures.

CS, IHCS, N₂, He and PP stand for cold spray, induction heating cold spray, nitrogen, helium, and particle preheating, respectively. The first part of the label indicates the process used for the production of the sample, CS or IHCS. The second part of the label represents the propellant gas used during the spraying process (nitrogen or helium). The third part of the label represents the use of controlled particle preheating. PP₁ and PP₂ represent 400 and 750 °C, respectively, as the initial injection particle preheating temperature. If PP is not used on the labels, then the initial injection particle temperature was 25 °C (Ref 35).

Sample Characterization

To characterize the coatings, scanning electron microscopy (SEM) (EVO MA-10, Carl Zeiss AG, Oberkochen, Germany) was used. The cross-sectional images of the coatings were obtained under the detection of backscattered electrons (BSD). To quantify the densification/porosity level of the deposits, the ImageJ software and the contrast imaging technique were used (Ref 46, 47, 51). The coatings microhardness was obtained using a Duramin-10 tester (Struers Aps, Denmark) equipped with a Vickers indenter using a load of 0.3 kg. Indentations were performed every 50 μm , from the coating/substrate interface up to the top region of the coatings. This process was repeated twice at different locations in a cross section, and the values were then averaged.

Fig. 3 Schematic of the IHCS setup. (a) Cross section and (b) top view

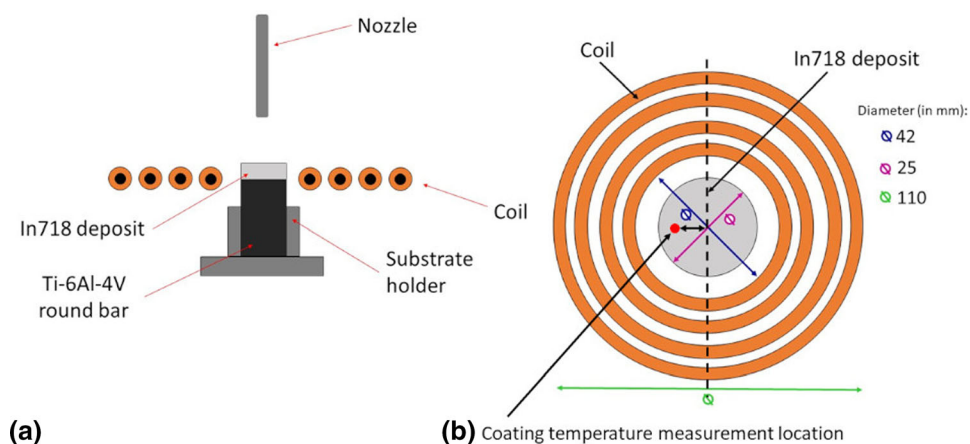


Table 2 Designation of the produced deposits

Label	Initial Temperature, °C	
	Particle	Coating
CS – N ₂	25	25
CS – N ₂ – PP ₁	400	25
CS – N ₂ – PP ₂	750	25
CS – He	25	25
CS – He – PP ₁	400	25
IHCS – N ₂	25	600
IHCS – He	25	600
IHCS – He – PP ₁	400	600
IHCS – N ₂ – PP ₂	750	600

Computational Fluid Dynamics (CFD)

In the CS process, the particles exiting the nozzle are characterized by their relatively low particle temperature and relatively high velocities. For these reasons, the use of classical optical pyrometry is not possible, and thus, any particle temperature measurement becomes a technical challenge or an extremely lengthy process. Recently, a computational fluid dynamics model has been developed to predict the particle impact velocity and temperature. This model has also been extensively validated using a Cold Spray meter and high-speed infra-red camera (Ref 14, 63). The model has been shown to be able to accurately predict the particle impact velocity and temperature. Therefore, in this work, the same extensively validated CFD model is used to predict the particle impact temperature and velocity. The commercially available Ansys Fluent 16 software was used to carry out the CFD model.

The predicted average particle impact velocity and temperature are used to calculate η value. Assadi et al. (Ref 36) first defined η as shown by Eq. 1:

$$\eta = \frac{V_{\text{impact}}}{V_{\text{critical}}} \quad (\text{Eq. 1})$$

where V_{impact} is the average particle impact velocity and V_{critical} is the critical velocity. This parameter has proven to be a valuable tool for predicting the ability of producing CS coatings. The critical velocity values for In718 are taken from the data reported by Perez-Andrade et al. (Ref 10). In this work, η is used as valuable indicator of what to expect in terms of the deposition based on the different spray conditions.

The three-dimensional model comprised by the nozzle and the spray chamber/substrate geometries was split into different computational domains and grids to accurately capture all the flow features, as shown in Fig. 4. The computational domain dimensions can be found in Table 3. The meshing process was carried out using the built-in Ansys Meshing Module. The sweepable mesh was used where the nozzle geometries allowed, otherwise a tetragonal mesh was used. A grid dependency study was carried out in which five meshes were tested: less than 100,000 elements, $\sim 200,000$ elements, $\sim 700,000$ elements, $\sim 900,000$ elements, and more than 1,000,000 elements. The model comprised of $\sim 900,000$ elements provided adequate results without compromising the computational time.

The Reynolds-Average Navier–Stokes (RANS) equations were used along with the re-normalized k- ϵ turbulence model (RNG k- ϵ) to model the gas flow (Ref 35, 52–54). Convergence was assumed to be reached when the residuals decreased by at least four orders of magnitude. As an additional criterion for convergence, a mass imbalance of less than 1% between the gas inlet and the nozzle exit was required.

At the nozzle inlet, the stagnation pressure and temperature were specified using the values presented in Table 1. At the inlet of the powder feeding line, a gas mass flow rate boundary condition was fixed. The gas mass flow

Fig. 4 Three-dimensional computational domain and meshing for the CS system. Computational domain dimensions can be found in Table 3

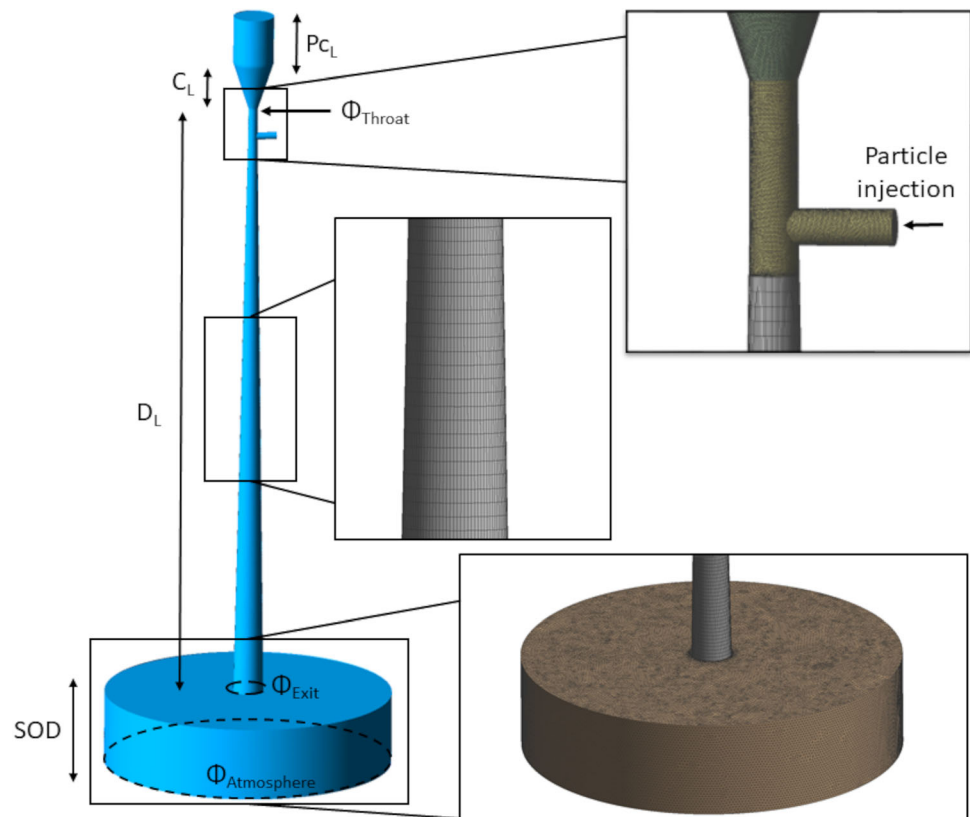


Table 3 Computational domain dimensions

CFD subdomain	Size, mm
Throat diameter (Φ_{Throat})	2
Surrounding atmosphere ($\Phi_{\text{Atmosphere}}$)	60
Nozzle exit diameter (Φ_{Exit})	6.3
Stand-off distance (SOD)	15
Pre-chamber length (P_{C_L})	10
Converging length (C_L)	10
Diverging length (D_L)	120

rate at the powder feeding inlet was 0.00033 kg/s. Three gas temperatures at the powder feeding line inlet were modeled: 25, 400 and 750 °C. Due to the long powder preheater tube length, it was assumed that by the time the particles were fed into the nozzle, their temperature had already reached the powder feeding gas temperature. The surrounding atmosphere at the end of the nozzle was set at room temperature and atmospheric pressure. A summary of the boundary conditions (BC) used in the CFD model is presented in Table 4.

The fluid and particle properties used in this CFD model are presented in Table 4. The values presented in Table 5 were selected based on the data available in the literature (Ref 1, 11, 35, 55–57).

A particle size distribution of 10 to 45 μm with an average size of 30 μm was used, as presented in Table 5. These values were selected as they correspond to the powder size distribution used experimentally. The effect of the particles on the gas phase and the particle–particle interactions were neglected because of the low volume fraction of the powder particles with respect of the gas flow (volume fraction < 10%) (Ref 52, 58–60). The different particle trajectories and their stochastic behavior inside the nozzle were taken into account by using the discrete random walk (DRW) model. The particles were injected in the divergent region of the nozzle, matching the injection location of the physical nozzle, as shown in Fig. 5. A minimum of 1000 particles were used to calculate the average particle impact velocity and temperature. An in-depth description of the validated computational model can be found elsewhere (Ref 35).

Results and Discussion

Particle Impact Temperature and Velocity

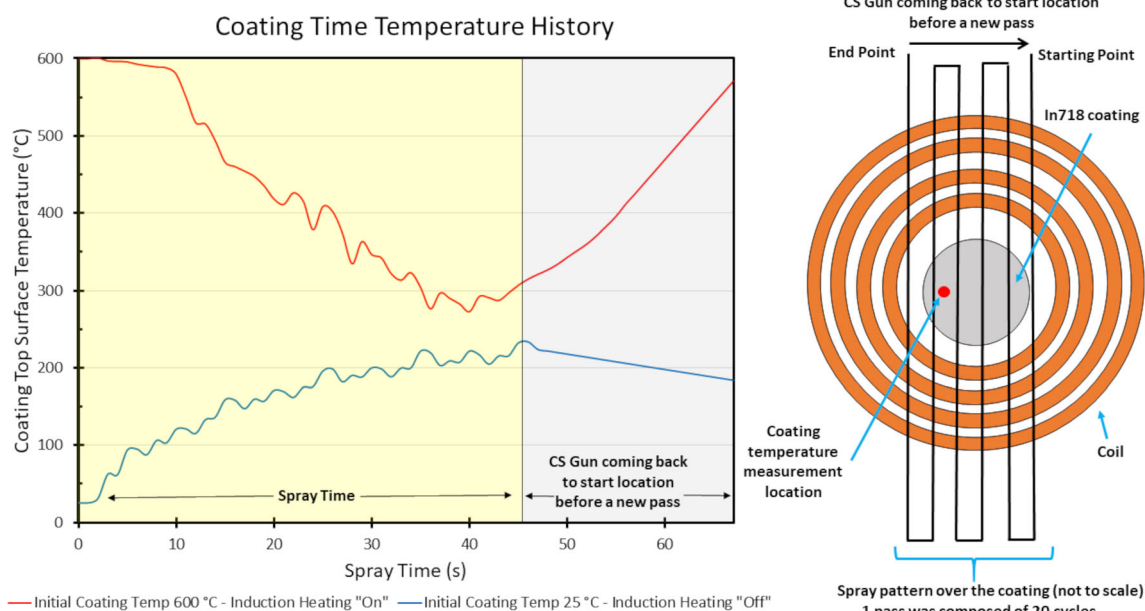
The predicted average particle impact velocity and temperature are presented in Table 6.

Table 4 Numerical model boundary conditions

Location	Type of BC	Temperature, °C		Pressure, MPa	
		Nitrogen	Helium	Nitrogen	Helium
Main gas inlet	Pressure inlet	Stagnation conditions		Stagnation conditions	
Powder inlet	Mass inlet	25, 400, and 750	400	N/A	
Surrounding atmosphere	Pressure outlet	25	N/A	Atmospheric	N/A
Substrate	Wall	Adiabatic		N/A	

Table 5 Properties used in the CFD model

Properties	Nitrogen gas	Helium gas	In718 particles
Particle size distribution, average size, μm	N/A	N/A	10–45, 30
Stagnation conditions	Available in Table 1		N/A
Density, kg/m^3	Ideal gas		8190
Specific heat capacity, J/kgK	1040.6	5192.6	435
Thermal conductivity, W/mK	0.0242	0.152	11.4
Viscosity, kg/m-s	Sutherland's law		N/A
Initial particle temperature at the injection location, °C	N/A	N/A	25, 400, and 750

**Fig. 5** Coating surface time–temperature history. Red curve: the induction heating system “On” during the spray time and initial coating temperature is 600 °C. Blue curve: induction heating system is kept “Off” during the spray time and initial coating temperature is

25 °C. A “pass” over the coating is completed by the time the nozzle has completed 20 cycles (cycle = 1 back and forth movement) (Color figure online)

Using nitrogen as the propellant gas accelerates the particles to an average V_{impact} of around 604 m/s. For this case, the average particle impact temperature is approximately 77 °C. At this temperature, V_{critical} is approximately 800 m/s (Ref 10). Thus, for the use of nitrogen as the propellant gas, an η equal to 0.75 was calculated. Consequently, minimal to no deposition is expected. The particle impact velocity for the cases in which the initial particle

temperature was increased to 400 and 750 °C is on average 590 m/s. For these cases, the average particle impact temperatures are 349 and 600 °C, respectively. The difference between the initial and the impact temperatures is caused by heat exchanged between the relatively cold gas in the diverging section and the warm particles. The benefit from increasing the particle impact temperature is visible in Table 6 as the critical velocity is reduced by approximately

Table 6 Predicted average particle impact velocity and temperature, and average η for the In718 powder

Propellant gas- T_0 (°C)- P_0 (MPa)-Initial particle temperature, °C	Particle Impact		Critical velocity, m/s (Ref 10)	η
	Velocity, m/s	Temperature, °C		
N ₂ – 500 – 3.45 – 25	604 ± 95	77 ± 25	802	0.75
N ₂ – 500 – 3.45 – 400	590 ± 102	349 ± 29	702	0.85
N ₂ – 500 – 3.45 – 750	590 ± 87	600 ± 66	598	0.98
He – 500 – 2.06 – 25	848 ± 168	139 ± 44	787	1.07
He – 500 – 2.06 – 400	845 ± 158	257 ± 49	739	1.14

25% (598 m/s vs 802 m/s). Despite this reduction, η was 0.85 and 0.98 and thus minimal deposition is also expected.

The use of helium in combination with initial particle temperatures of 25 and 400 °C leads to a predicted average particle impact velocity of approximately 850 m/s for both cases. The higher average particle impact velocity values are caused by the low molecular weight and high specific heat ratio of helium in comparison to nitrogen, resulting in considerably higher gas velocities (Ref 31, 32, 51, 61–65). The predicted average particle impact temperatures for the feeding gas temperatures of 25 and 400 °C were 139 and 257 °C, respectively. Based on the predicted values, particles are likely to deposit under these two spray conditions as their η is slightly above 1 (Table 6). In the literature, an $\eta = 1.5$ has been used as a benchmark that ensures dense copper coatings (Ref 36), but a clear benchmark for the deposition of an In718 dense coating has not yet been established.

Coating Surface Time–Temperature History

In a previous work (Ref 46), measuring the substrate time–temperature history provided insightful information to better understand the influence of this temperature on the CS deposition process. For that reason, a similar approach is followed and the coating surface time–temperature history is monitored for two initial coating temperatures: 25 and 600 °C. Figure 5 presents the coating surface time–temperature history for one nozzle pass over the coating surface using nitrogen as a propellant gas.

The blue curve in Fig. 5 represents the coating surface time–temperature history for the case in which the induction heating system is “Off” during the spray time. The coating surface temperature exhibited an increasing trend, with some noticeable fluctuations, attributed to the nozzle scanning pattern over the coating surface (Ref 46, 47). This trend is caused by the convective heat transfer between the impinging gas stream and the coating combined with conduction heat transfer through the coating thickness and substrate. The gas flow should decelerate on the coatings

surface bringing the gas back to the stagnation conditions. However, losses associated with a non-isentropic and non-reversible process contribute to a lower stagnation gas temperature than the initial temperature. By the end of the nozzle pass, the coating heating rate tends to stabilize pointing to a “steady-state” coating temperature at around 225 °C, lower than the initial gas temperature (500 °C) (Ref 46, 66–69). This result suggests that the maximum temperature a coating could reach is about 50% of the stagnation temperature. The primary reason driving the use of high stagnation temperatures for the deposition of In718 coatings is higher particle impact velocities and temperatures. By monitoring the coating surface time–temperature history, it can be concluded that another benefit of the use of high stagnation temperatures is inducing thermal softening on the already deposited coating layers. Using stagnation temperatures ranging 600–1000 °C could potentially increase the coating temperature to values between 300 and 500 °C favoring coating densification, reducing the critical velocity for deposition, and thus, increasing the DE.

The red curve presented in Fig. 5 represents the coating surface time–temperature history for the case in which the IH system is “On” during the spray time. The coating experienced a cooling effect because the initial temperature was above the “steady-state” temperature (225 °C), as expected based on previous results (Ref 46, 47). The fluctuations are also attributed to the nozzle scanning pattern over the coating surface and the relatively low thermal conductivity of In718. These fluctuations become more evident as the nozzle approaches the measurement location. During most of the spray time, the heat exchange between the gas stream and the coating surface was dominant over the heating rate of the induction heater. However, in the last few seconds, when the nozzle was about to leave the coating surface, it can be seen that the coating temperature started to ramp up. By the time the nozzle was about to start a new pass of the deposition process, the coating temperature had already reached about 95% of the initial coating temperature (600 °C). Based on the trend

shown by the red curve, to achieve similar coating surface temperatures, the stagnation temperatures near the 1000 °C range would be needed to achieve a similar effect. The different coating surface time–temperature histories shown in Fig. 5 are expected to produce a significant difference in the deposition process because the particles will impact on average a softer coating in comparison to the case represented by the blue curve (Ref 46, 47).

Effect of the Particle Impact Temperature and Impact Velocity

Before investigating the influence of the coating temperature on the production of In718 coatings, the influence of the particle impact temperature and velocity is first investigated.

Using nitrogen as the propellant gas and three different initial particle temperatures: 25, 400 and 750 °C (with an average predicted particle impact temperature of 77, 349 and 600 °C, respectively) resulted in minimal deposition (DE less than 1%), as presented in Fig. 6(a–c), respectively. Increasing the particle impact temperature reduced the critical velocity, and thus, the η value increased from a minimum of 0.75 to a maximum of 0.98. For the three cases (CS – N₂, CS – N₂ – PP₁ and CS – N₂ – PP₂) only a first layer of particles was able to adhere to the substrate, most likely through mechanical interlocking with no subsequent layers being built. The particles of these single-layer coatings were well deformed as a consequence of the repeated impingement of the incoming non-adhering particles.

A drastic increase in coating thickness (Fig. 7) was obtained when using helium, due to the higher η value (1.07) experienced by the impacting particles. The In718 particles had more kinetic energy prior to impact to break

their native oxide layer, deform, and bond. The thick CS – He sample shows a relatively low porosity (< 1%). While the particles reached significantly higher impact velocities (approximately 40% higher in comparison to nitrogen), micro-cracks parallel to the substrate/coating interface and scattered across the coating cross section were visible.

The CS – He – PP₁ sample (Fig. 8) is significantly thicker than the sample without particle preheating. As predicted by η (Table 6), the higher particle impact temperature improved the DE, from 8 to 17%, as presented in Table 7, with the coating thickness increasing accordingly by about 50%. The increased particle impact temperature facilitated localized deformation (adiabatic shear instabilities) at the region close to the particle surface, and promoted the particles to meet the minimal conditions required for bonding (Ref 34, 35). However, the coating porosity level increased from < 1% to close to 2%. The latter is not something that could have been predicted for a higher η value. However, increasing the particle impact temperature

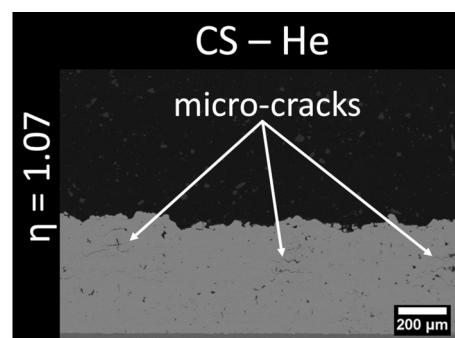
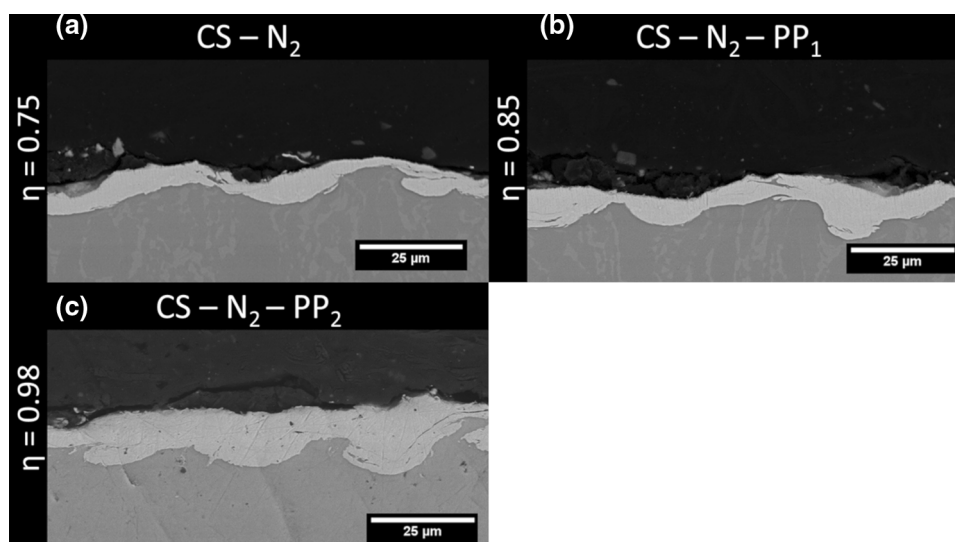


Fig. 7 Cross-sectional images of CS – He coating. CS and He stand for cold spray and helium, respectively. If PP is not used on the labels, then the initial injection particle temperature was 25 °C

Fig. 6 Cross-sectional images of the different coatings produced in this study. CS, N₂, and PP stand for cold spray, nitrogen, and particle preheating, respectively. PP₁ and PP₂ represent 400 and 750 °C, respectively, as the initial injection particle preheating temperature. If PP is not used on the labels, then the initial injection particle temperature was 25 °C



has eliminated the presence of micro-cracks, as observed in Fig. 7 vs. 8.

Even though successful deposition was achieved using helium as the propellant gas (CS – He), additional micro-cracks appeared at the vicinity of the mark left by the indenter after completing the micro-hardness measurement, as shown in Fig. 9(a). The presence of cracks induced by micro-hardness testing have also been observed in as-sprayed In718 coatings when elevated spray parameters (800 °C and 3.5 MPa) were used (Ref 13). The appearance of these cracks has been proposed as an indicator of weak inter-particle bonding, limited particle deformation and a low coating quality (Ref 13, 70).

Even though the initial particle temperature was set to 400 °C (with a particle impact temperature of approximately 260 °C), superior inter-particle bonding was not achieved, as confirmed by the cracks that appeared in the vicinity of the indentation mark shown in Fig. 9(b), suggesting limited plastic deformation that lead to porosity and reduced cohesion (Ref 13, 70). Additionally, more cracks are visible in comparison to Fig. 9(a). The higher number of cracks is potentially caused by the numerous pores inside the coating (Fig. 8). Porosities act as stress concentrators facilitating crack propagation through the

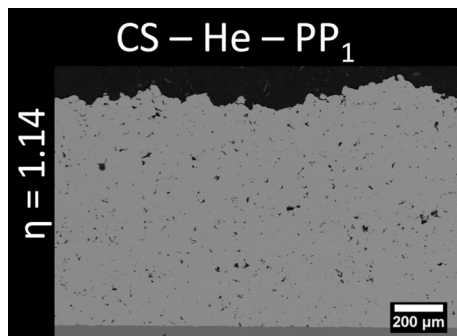


Fig. 8 Cross-sectional images of the CS – He – PP₁ coating. CS, He and PP stand for cold spray, helium, and particle preheating, respectively. PP₁ represents 400 °C as the initial injection particle preheating temperature

weakest points of the coating (particle-to-particle interfaces). The similar micro-hardness values, available in Table 7, between the CS – He and CS – He – PP₁ coatings also support this observation.

To summarize the effect of particle impact temperature and velocity during the cold spraying process of spherical metallic powders, Fig. 10 (adapted from (Ref 40)) presents the DE and densification level % (100 – porosity level) values for pure aluminum as a function of the average particle impact velocity. The variation of particle impact temperature was not monitored or considered in that study (Ref 40).

The first consolidation behavior (Type I) occurs in the region where low particle impact velocities result in lower DEs and higher densification (low porosity) values, as presented in Fig. 10(a) and (b). In this zone, plastic deformation of the few adhering particles is promoted by the many particles impacting on and bouncing off the adhered particles. This closes the pores and densifies the consolidated material (impingement effect) (Ref 40). As the average particle impact velocity increases, the DE increases. However, this reduces the impingement effect resulting in a reduced densification level of the consolidated material (Ref 40). The second consolidation behavior (Type II) is characterized by a simultaneous increase in both DE and densification level. In that region, the main densification mechanism is attributed to the extensive plastic deformation that the particles experience directly upon impact (Ref 40).

The previous trends have also been observed for spherical aluminum alloy, stainless steel, and CoNiCrAlY (Ref 51). Therefore, it is likely that all spherical metallic powder materials display these two consolidation behaviors. The trends presented in Fig. 10 are shown schematically for, in theory, any feedstock powder material in Fig. 11(a) and (b) (red curves). The red curves have been created by curve fitting a trend to the experimental results presented in Fig. 10(a) and (b).

Based on the estimated particle impact velocity and the η values presented in Table 6, the particles examined so far

Table 7 Characteristics of In718 coatings. CS, IHCS, He and PP stand for cold spray, induction heating cold spray, nitrogen, helium, and particle preheating, respectively. PP₁ represents 400 as the initial

injection particle preheating temperature. If PP is not used on the labels, then the initial injection particle temperature was 25 °C

Label	Thickness, μm	Micro-hardness, HV	DE, %	Porosity, %
CS – He	461 ± 21	469 ± 26	8.0 ± 0.4	< 1
CS – He – PP ₁	907 ± 28	460 ± 25	17.2 ± 0.5	~ 2
IHCS – He	230 ± 23	N/A*	4.1 ± 0.2	N/A*
IHCS – He – PP ₁	508 ± 33	537 ± 28	10.4 ± 0.4	< 1

*The micro-hardness and porosity are not available (N/A) because the coating contained too many cracks

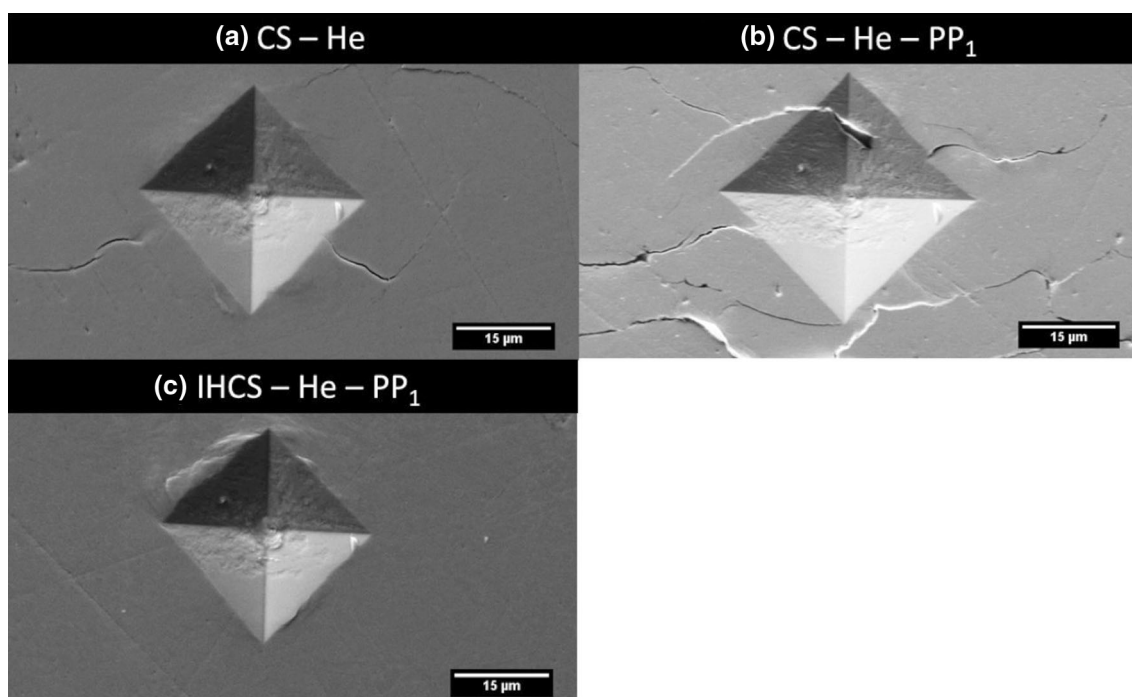


Fig. 9 SEM image of the mark left on the samples by the microhardness indenter. CS, IHCS, He and PP stand for cold spray, induction heating cold spray, helium, and particle preheating,

respectively. PP₁ represents 400 °C as the initial injection particle preheating temperature. If PP is not used on the labels, then the initial injection particle temperature was 25 °C

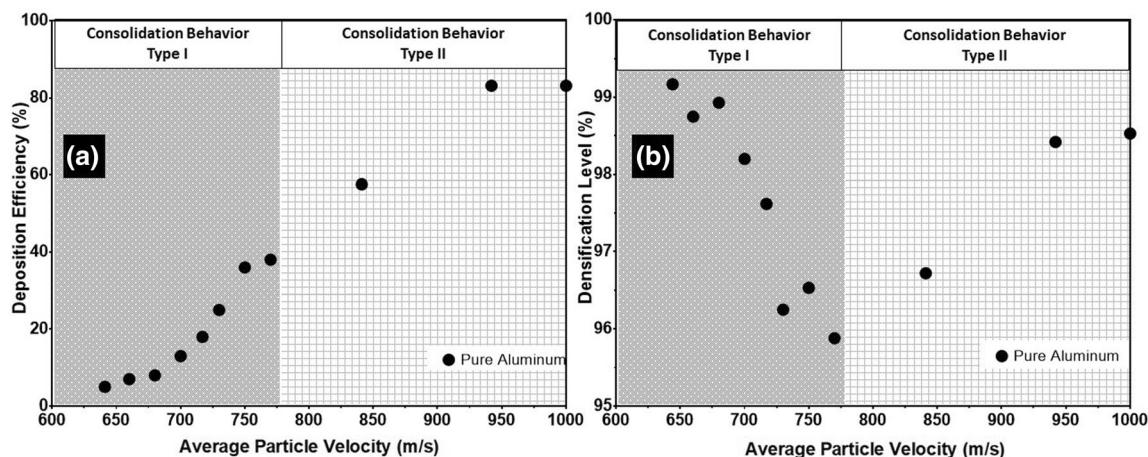


Fig. 10 (a) Deposition efficiency and (b) densification values of pure aluminum coatings as a function of the average particle impact velocity. The data points for spherical pure aluminum were taken and adapted from (Ref 40).

in the current work were likely sprayed in the “Consolidation Behavior Type I” region, further supported by the low DE values registered. Consequently, the densification process observed and reported in Table 7 must be controlled by the impingement effect (Ref 40, 71).

Figure 11(a) and (b) presents the effect of particle preheating on the trends of DE and densification levels as a function of the average particle impact velocity (green curves). The green curves follow the same curve-fitted trend for the red curves. The DE curve (CS – PP) in

Fig. 11(a) has been shifted to the left from its original position (red curve). This shift occurs because higher particle impact temperatures reduce the critical velocity for deposition as particle deformation is facilitated (Ref 34–37, 72–74). A good example of this is demonstrated by Eq. 2 (Ref 36), which expresses the critical velocity of copper, only, as a function of the material properties and particle temperature:

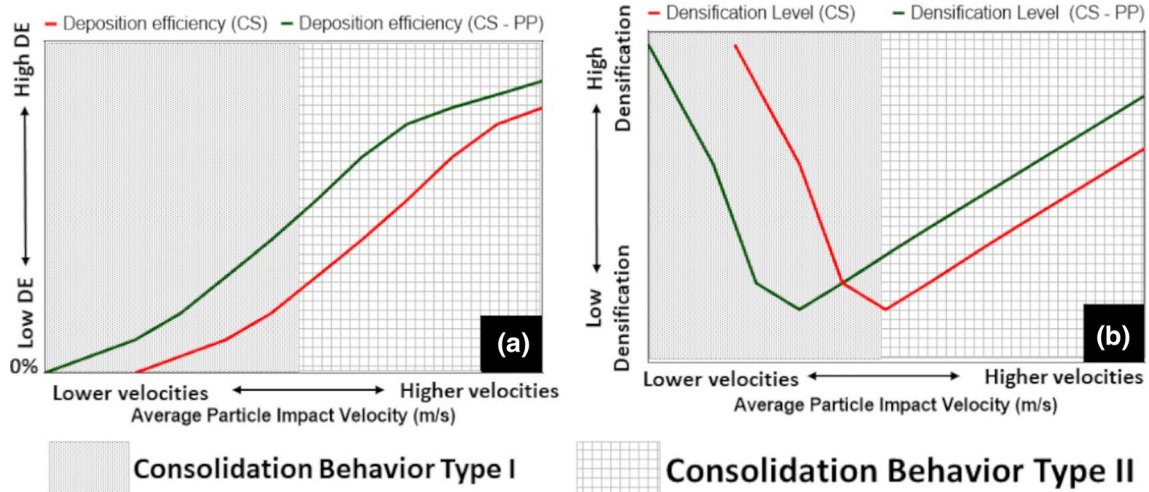


Fig. 11 Consolidation behavior as a function of the average particle impact velocity and particle preheating. In (a) DE and in (b) densification level as a function of the average particle impact velocity and particle preheating (higher particle impact temperature). The red

curves represent the CS process, while the green line indicates the effect of particle preheating on the CS process (CS – PP) (Color figure online)

$$V_{\text{critical}} = k_1 \sqrt{c_p(T_m - T_p) + 16 \frac{\sigma}{\rho_p} \left(\frac{T_m - T_p}{T_m - 293} \right)} \quad (\text{Eq 2})$$

In Eq. 2, k_1 is a particle size-dependent dimensionless fitting parameter, C_p is the specific heat of the particle material, T_m is the particle material melting temperature, T_p is the particle impact temperature, σ is the tensile strength of the particle material at 293 K, and ρ_p is the particle density. In the literature, this equation has been used to describe how the critical velocity behavior for other materials, and it is widely accepted that the critical velocity is a function of the particle temperature. Therefore, warmer particles are likely to deposit at lower velocities, producing higher DE values for a similar average particle impact velocity (Ref 34–37, 72–74).

A common knowledge of the CS field is that increasing the particle impact temperature will improve the coating density (decrease the coating porosity). This has driven the use of elevated spray parameters in the CS field, and more particularly their use for the deposition of In718 (Ref 9–26). However, in the “Consolidation Behavior Type I” region of Fig. 11(b) for a specific impact velocity, the densification level of a coating decreases (green curve) in comparison to particles at lower impact temperatures (red curve). In this zone, higher particle impact temperatures are enough to promote localized deformation (adiabatic shear instabilities) at the region close to the particle surface, but not enough to promote extensive deformation of the entire particles. This enhances particle bonding and leads to an increased DE, but reduces the impingement effect and the pores created

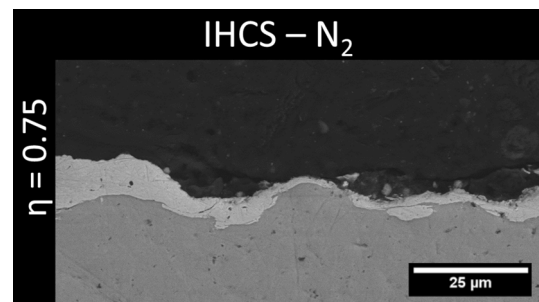


Fig. 12 Cross-sectional images of the IHCS – N₂ coating. IHCS and N₂ stand for induction heating cold spray and nitrogen, respectively. If PP is not used on the labels, then the initial injection particle temperature was 25 °C

due insufficient overall particle deformation are left open (Ref 40, 71). This behavior explains the increase in porosity (decrease in densification) for the CS – HE – PP sample with respect to the CS – HE coating. An increase in the porosity levels have also been observed for the deposition of Al-Si and MCrAlY when the particle impact temperature increased (Ref 38, 39).

In the “Type II” region of Fig. 11(b), the powder preheating curve (green curve) shows higher densification values with respect to the curve without powder preheating (red curve). The higher values for the green curve in Fig. 11(b) are caused by the combination of relatively higher particle impact temperatures and velocities, which both enhance plastic deformation, and thus, densification upon impact. In other words, the “Type II” region demonstrates why elevated spray parameters are commonly associated with the production of a less porous coating (Ref

10, 14, 19, 21, 40, 75–82). Ultimately, Fig. 11(b) unifies the very different results that have been reported for the effect of the particle impact temperature on the coating quality.

Effect of the Coating Temperature and Particle Impact Velocity

As a first step to investigate the effect of the coating (or already deposited layers) temperature on the CS deposition of In718, an initial coating temperature of 600 °C, an injection particle temperature of 25 °C, and nitrogen as the propellant gas were used. This combination of spray parameters resulted in a thin coating similar to the one produced for an initial coating temperature of 25 °C, as shown in Fig. 12, and the DE was less than 1%.

Based on the significant higher average coating temperature reported in Fig. 5 (red curve), these results were unexpected because, for aluminum, higher coating temperatures produced significant increases in DE and coating thickness (Ref 46). In previous work, the drastic changes in DE were attributed to a reduction in the critical velocity as a result of the local heating process of the coating layers by the eddy current density distribution resulting from the induction heating (Ref 46). As a result, the incoming particles impacted thermally softened coating layers. This promoted more particles to meet conditions for bonding, and thus, higher deposition rates were obtained (Ref 46). However, while Fig. 5 confirms that the particles impacted a warmer (thus softer) coating, in Fig. 12 only a slight effect can be seen in comparison to Fig. 6(a). The slight difference is attributed to the higher initial substrate temperature, which had a limited effect to only the first layer of deposited particles (Ref 47). The samples presented in Fig. 6(a) and 12 were produced using identical spray parameters and because of that η was 0.75. While the coating temperature at the end of the time–temperature history was relatively high (570 °C) (based on Fig. 5), this coating temperature was not high enough to produce an

enhanced thermal softening that could promote a drastic reduction in the critical velocity. To potentially further reduce the critical velocity of In718, and based on its mechanical properties, coating temperatures beyond 650 °C are needed. Therefore, the induction heating parameters must be re-evaluated and assessed. It is likely that by increasing the current from the IH to higher values, a superior coating heating process can be achieved resulting in a more noticeable reduction in the critical velocity. Higher coating temperatures would promote particle entrapment in the coating upon impact, as observed for aluminum in a previous work (Ref 46).

To further investigate the influence of the coating temperature on the CS deposition process, the particle velocity was increased by using helium as the propellant gas, the initial coating temperature was set at 600 °C, and no powder preheating was used ($\eta = 1.07$). Despite having an identical η value (IHCS – He vs CS – He), which in theory should result in similar deposition behavior, the IHCS – He coating (Fig. 13) was approximately 50% thinner than the one produced without the use of IH (Table 7).

Additionally, previous studies focused on the deposition of In718 have reported successful consolidation of crack-free and dense coatings using average η values < 1.15 (Ref 11, 26). The identical η values between the IHCS – He vs CS – He samples and the results reported in the literature suggest that the coating temperature can significantly influence the CS deposition process. The η value is traditionally a sound indicator to predict the deposition behavior, but it does not include information about the substrate/coating temperatures and their effect on the overall coating quality. It is believed that the thinner coating is likely caused by the dissimilar deformation behavior between the thermally softened coating layers and the incoming hard particles. For the CS – He sample (Fig. 7), hard particles were sprayed on relatively hard coating layers. By increasing the coating temperature (using the IH process), the incoming hard particles impacted warmer coating layers (the coating temperature can be estimated between 300 and 600 °C based on Fig. 5) compared to the case without using IH. However, the coating temperatures were likely not high enough to promote particle embedment and increase the DE during the spraying process. Instead the relatively high coating temperatures restricted the particle deformation because their kinetic energy was mostly dissipated into deformation of the relatively softer counterpart, as first suggested by Bae et al. (Ref 83). It is believed that based on the mechanical properties of In718, coating temperatures above 650 °C would be needed to produce sufficient local coating deformation that would lead to particle embedment in a similar way than the one observed for aluminum (Ref 46, 47). With the current coating temperatures that can be achieved using the maximum parameters

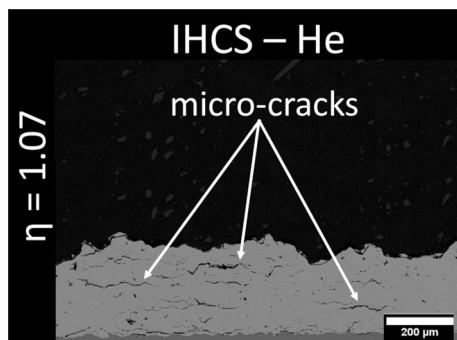


Fig. 13 Cross-sectional images of the IHCS – He coating. IHCS and He stand for induction heating cold spray and helium, respectively. If PP is not used on the labels, then the initial injection particle temperature was 25 °C

of the IH system, higher impact velocities would be required to penetrate into the already deposited coating layers, deform, and produce a similar coating thickness as the one obtained for the CS – He sample (Ref 83). This transition in the deformation behavior between the coating layers and the incoming particles is likely to be more pronounced as the powder material strength increases. For that reason, this effect was likely not observed during the deposition of a soft powder (pure aluminum) (Ref 46).

In addition to the lower deposition rates, increasing the coating temperature also had a detrimental effect on the consolidated material as large cracks between layers can be observed in Fig. 13. To explain these cracks, it is important to first consider that the samples without coating heating had already exhibited weak inter-particle bonding, as shown in Fig. 7 and 9(a). Additionally, the coating experiences quick heating caused by the IH system (heating rate of ~ 11 – 12 °C/s) and rapid cooling (~ 12 °C or higher as this sample had helium as the propellant gas) due to heat exchange between the propellant gas during each nozzle pass over the coating surface (Fig. 5). In the CS process, the presence of thermal residual stresses is not significant due to the relatively low coating temperatures (Ref 84), and experimental values associated with thermal residual stresses are often around 100 MPa for Inconel 718 coatings (Ref 10, 17, 18). However, knowing that thermal stresses become significant at coating temperatures above 400 °C (Ref 84–86), as in this work (Fig. 5), a theoretical value for these can be approximated to 1 GPa ($\sigma = E\alpha(T_i - T_f)$), if $E = 200$ GPa, $\alpha = 12.8 \times 10^{-6}$, $T_i = 600$ °C, and $T_f = 200$ °C. This value is superior to any potential coating cohesion strength value reported in the literature. While the theoretical value provides a first approximation of the maximum expected value, it has been shown that various stress-relaxation mechanisms operate within the coating reducing the maximum tensile stress values (Ref 87), as reported by Barton (Ref 44). Based on these conditions and the In718 low thermal conductivity and relatively high thermal expansion

coefficient, tensile residual stresses are likely developed and these potentially overcame the cohesion strength of the coating creating defects such as the cracks shown in Fig. 13.

Effect of the Coating Temperature, Particle Impact Temperature and Impact Velocity

To further study the relationship between the coating temperature and the particle impact temperature and velocity, nitrogen was used as the propellant gas, the initial particle temperature was increased to 750 °C, and the initial coating temperature was set at 600 °C. Similarly, as for the IHCS – N₂ sample, the IHCS – N₂ – PP₂ sample was mainly composed of one or two particles at most, as shown in Fig. 14. Even though the critical velocity is likely a function of the coating temperature, for the current temperature values, the benefit of higher coating temperatures is not sufficient to obtain a significant build up.

To increase the particle impact velocity, helium was used. Additionally, to minimize powder/coating hardness differences while maximizing the coating quality and DE using the available maximum IH power output and spray parameters available on the commercial CS system used in this work, powder preheating was set at 400 °C. In Fig. 15, a representative cross-sectional image of the sample (IHCS – He – PP₁) produced using the IHCS, with helium as the propellant gas and powder preheating is presented.

A crack-free coating was obtained with an average thickness of 508 μm (Table 7). The coating porosity was within or below the reported range of values obtained using high spray parameters (Ref 10, 11, 13–17, 17, 19, 21–23, 26) as well as lower compared to APS (Ref 8) and HVOF (Ref 5). The samples presented in Fig. 8 and 15 had an identical η value (1.14), but the coating quality was significantly different. While η is an excellent tool to estimate particle deposition, the equation to calculate η might be incomplete and terms should be added to account

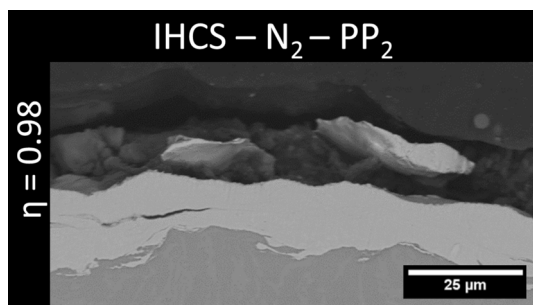


Fig. 14 Cross-sectional images of the IHCS – N₂ – PP₂ coating. IHCS, N₂, and PP stand for induction heating cold spray, nitrogen, and particle preheating, respectively. PP₂ represents 750 °C as the initial injection particle preheating temperature

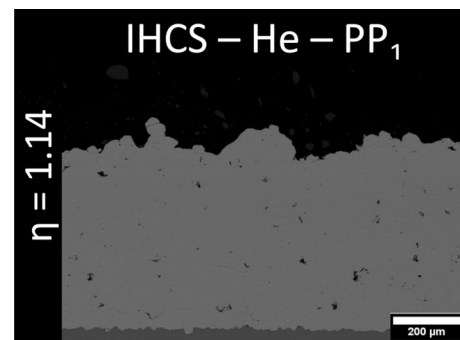


Fig. 15 Cross-sectional images of the IHCS – He – PP₁ coating. IHCS, He, and PP stand for induction heating cold spray, helium, and particle preheating, respectively. PP₁ represents 400 °C as the initial injection particle preheating temperature

for the influence of the coating and substrate temperatures, as the results have suggested until this point. Additionally, the IHCS – He – PP₁ sample (Fig. 9c)) exhibited a superior inter-particle bonding in comparison to any of the other samples presented in Fig. 9, as no cracks appeared in the surrounding area of the mark left by the indenter after the micro-hardness testing procedure. The average micro-hardness was 537 HV (Table 7) showing good agreement with the reported micro-hardness values for cold-sprayed In718 coatings (Ref 13, 16, 17, 19, 22).

The IHCS – He – PP₁ sample shows the benefit of increasing both the particle and coating temperatures toward the production of a high quality coatings. Increasing the particle temperature reduces the potential temperature difference between the coating layers and the impacting particles. Consequently, the softer coating layers and

particles were able to deform more similarly, even at low η values, enhancing the inter-particle bonding (as demonstrated by Fig. 9c)). Additionally, the particles were still “hard” enough to produce significant peening on the thermally softened coating layers further increasing the coating cohesion strength and reducing the coating porosities. The higher coating temperatures produced by the IH system are also likely to have enhanced the coating cohesion strength by producing an in situ heat treatment as temperatures between 300 and 600 °C are likely reached, as shown in Fig. 5. While some tensile residual stresses might still be present in the coating, due to the rapid cooling and heating caused by the propellant gas and IH heating rate, respectively, the coating cohesion strength was strong enough to avoid the development of internal coating cracks. A future study will be dedicated to evaluate

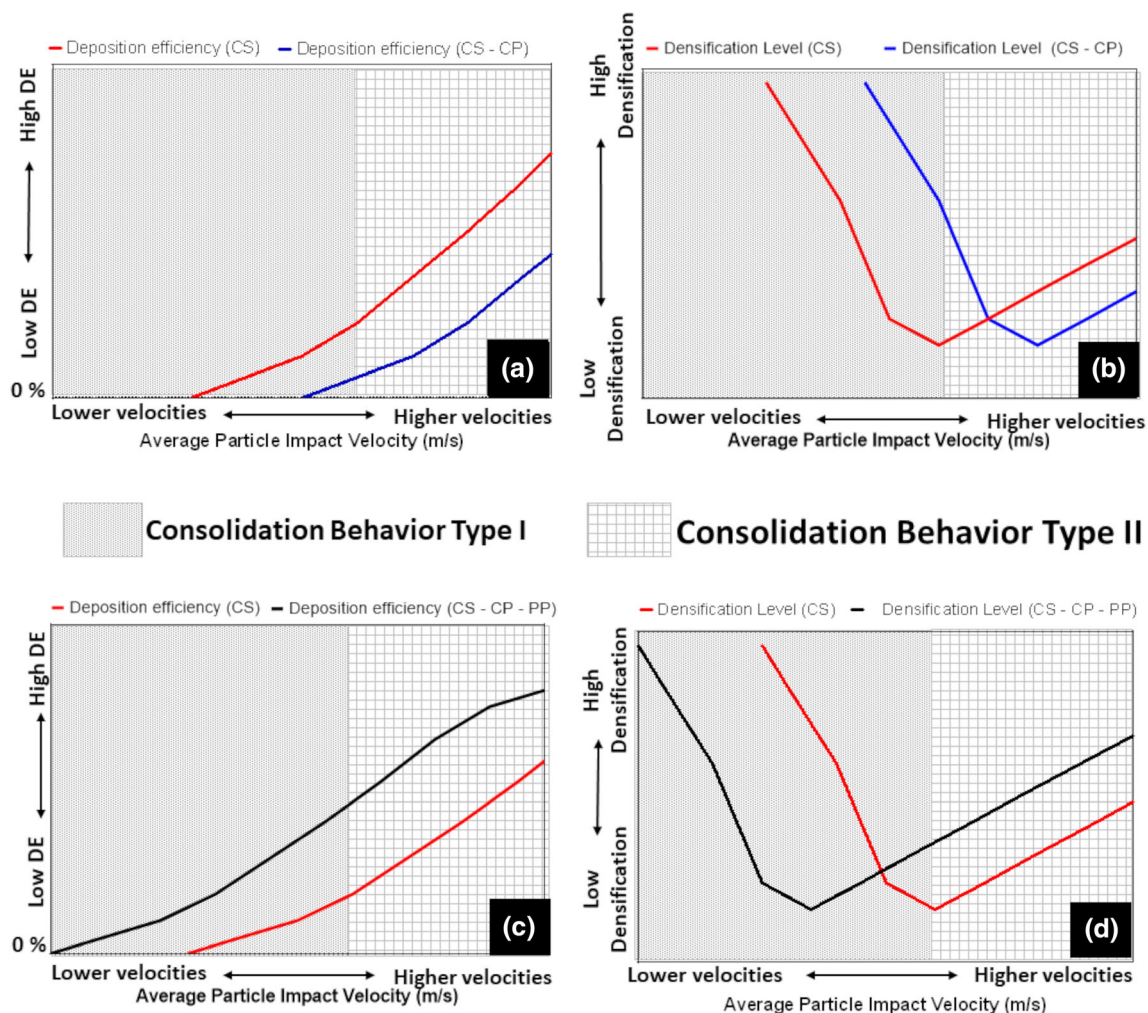


Fig. 16 Consolidation behavior as a function of the average particle impact velocity, coating and particle temperatures. In (a) and (c), DE, and in (b) and (d) densification levels are presented. In (a) and (b), the effect of the and coating temperature as a function of the average particle impact velocity on the deposition process is presented. In (c) and (d), the combined effect of the coating and particle impact

temperatures is also included. The red curves represent the CS process, while the blue curves (CS – CP) indicate the effect of the coating temperature on the CS process. CP stands for coating preheating. The black curve (CS – CP – PP) indicates the combined effect of coating and particle temperatures on the CS process (Color figure online)

the residual stresses inside the coating due to the rapid cooling and heating caused by the propellant gas and IH heating rate.

A summary of the effect of the coating temperature during the cold spraying process of spherical metallic powders is presented in Fig. 16(a) and (b). The blue curves follow the same curve-fitted trend for the red curves.

The shifting of DE to the right (blue curve, CP stands for coating preheating) from its original position (red curve) in Fig. 16(a) is attributed to the coating layers acting as a soft material in comparison to the hard particles. This follows the behavior first suggested by Bae et al., in which higher impact velocities are required to start depositing the particles when the hard-on-soft material combination is used (Ref 83). In this material combination, the soft material experiences most of the plastic deformation. However, due to the very limited plastic deformation that the particles may experience, the native oxide layer covering them is potentially not broken. While high-interfacial pressures might be reached at the particle/coating interface, it has been demonstrated that fresh and oxide-free surfaces at these two surfaces are needed to ensure bonding. Therefore, for the hard-on-soft material combination, unless high coating temperatures promote enough coating deformation for particle embedment, increasing the coating temperature can lead to lower DE values. This hypothesis was experimentally observed because the DE of the IHCS – HE coating decreased by 50% in comparison to the CS – He sample.

In Fig. 16(b), the “Type I” region is characterized by relatively low average particle velocities, as in this work. This region predicts an increase in the densification level when the coating temperature is increased (blue curve) in comparison to the CS process (red curve). In this zone, the impingement effect is maximized by dissimilar hardness of the coating and the particles. As a result, deformation on the coating layers is enhanced closing the remaining pores. An analogous effect has been reported by adding secondary hard particles to a soft powder matrix. The material mixture results in an “in situ shot-peening” effect that densifies the coating during the deposition process (Ref 22, 88–90). Promoting the impingement effect on the thermally softened coating layers by the hard particles is unquestionably beneficial as the porosities are reduced. However, for this particular powder material, the by-product of using this approach is the creation of a relatively dense coating with cracks between layers (Fig. 13). The relatively dense coating presented in Fig. 13 is obtained due to the repetitive impingement of the relatively hard particles on the soft coating layers promoting coating deformation and closing the remaining pores. The micro-cracks are potentially caused by the quick heating caused by the IH system and rapid cooling due to heat exchange between the propellant

gas during each nozzle pass over the coating surface. These conditions and In718 low thermal conductivity and relatively high thermal expansion coefficient promote tensile residual stresses that overcome the cohesion strength of the coating.

To illustrate the combined influence of the coating and particle impact temperatures on the consolidation behavior of In718, Fig. 16(c) and (d) is used. The black curves follow the same curve-fitted trend for the red curves. The curves labeled as CS – CP – PP (black lines, CP stands for coating preheating) are shifted to the left from the CS process curve (red curve) because increasing the coating and particle impact temperature (thus softening them both) reduces the critical velocity (Ref 34, 35, 46, 91). In Fig. 16(c) the CS – CP – PP curve illustrates higher DE values in comparison to the CS curve (red line), as observed experimentally and presented in Table 7. This demonstrates that the material strength (hardness) plays an important role when the coating temperature is increased. In a previous work focused on the deposition of aluminum, the material hardness difference between the coating layers and the sprayed particles, as in this work, was not observed because aluminum is an extremely soft and ductile material (Ref 46). However, for In718, increasing the particle impact temperature reduced the particle strength. In consequence, the hardness difference between the particles and the coating layers was reduced. This favored a similar deformation behavior leading to the creation of fresh and oxide-free surfaces between coating/particles promoting bonding. Once the hardness difference was reduced between the coating layers and the particles, a reduction in the critical velocity was obtained demonstrating the benefit of increasing the coating temperature. In the current work, the impingement effect controlled the densification of the coating. Thus, any increase in DE must come at the expense of increasing the pores inside the coating, as presented in Fig. 16(d) for the “Type I” region. Experimentally, the porosity level of the CS – He and the IHCS – He – PP₁ samples remained similar for both samples as the values were less than 1%. The similar porosity values are attributed to the resolution of the contrast imaging technique used to calculate the porosity values.

In the “Type II” region of Fig. 16(d), the black curve (CS – CP – PP) illustrates a continuous increase in the densification of the coating in comparison to the CS curve (red one). This portion of Fig. 16(d) shows the benefit of coupling the IH and the CS process because a higher coating quality (cohesion strength) in combination with higher deposition rates can be achieved. This portion of Fig. 16(d) was not explored in this work, but based on the extensive mapping reported in (Ref 51) for pure aluminum and DE and porosity values reported in (Ref 46), the predicted trend can be validated.

The need to use higher coating and particle impact temperatures would suggest that there is no benefit in the use of reduced spray parameters because a similar coating to the IHCS – He – PP₁ (Fig. 15) could potentially have been achieved using high spray parameters. However, the added benefit of decoupling the coating temperature from the gas stagnation temperature and fully controlling the coating temperature results in an improvement in the mechanical properties (Ref 47). It has been demonstrated that the adhesion, cohesion, and tensile strength can be tailored and greatly enhanced by independently increasing the coating temperature during the spray process (Ref 47, 49). Tailoring the coating mechanical properties using high spray parameters is impossible, because these properties are intrinsically tied to the spray parameters used for the coating fabrication. Additionally, having independent control of the coating and particle impact temperatures eliminated the persistent nozzle clogging issue that has been reported for the deposition of In718 powders (Ref 10, 14, 16, 19).

Conclusions

The effect of both particle and coating temperatures on the deposition of In718 and the exploration of the effect of using reduced spray parameters were studied. To ensure proper characterization, these temperatures were decoupled from the gas stagnation temperature (and consequently from impact velocity).

The influence of the particle impact temperature on the coating quality (DE and porosity levels) was linked to the particle impact velocity. For relatively low particle impact velocities, as in this work, higher particle impact temperatures increase the DE while also increasing the coating porosity. This is due to the fact that particle impingement is the main consolidation mechanism under these conditions. For high particle impact velocities, higher particle impact temperatures increase the DE and reduce the coating porosity values as the particles deform appropriately at impact, and this is enhanced with superior particle impact temperatures.

Independently of the particle impact temperature, and as opposed to previous results when pure aluminum was used as feedstock powder, the coating temperatures achieved in this work were not large enough to drastically reduce the critical velocity for deposition when nitrogen (and low spray parameters) was used. Higher coating temperatures than the ones achieved would be needed to significantly reduce the In718 critical velocity and promote particle embedment into the coating.

Helium was used as propellant gas at reduced spray parameters (stagnation gas pressure and temperature). On

the one hand, it was shown that solely elevating the coating temperature has a negative impact on the CS process. Elevating the coating temperature results in particle impact energy mostly dissipated into the deformation of the softer coating, while the hard particles experience reduced deformation generating weak inter-particle bonding and the formation of internal cracks. On the other hand, a simultaneous increase in the particle impact and coating temperatures reduced the hardness difference between the powder and the coating as well as the powder critical velocity. This produced an increase in the DE and enhanced the inter-particle bonding with coating porosity levels within or below reported values using higher CS parameters than the ones used in this work. Superior cohesion was also obtained due to the higher coating temperatures.

Acknowledgments The authors would like to thank Dr. Michel Nganbe for facilitating the use of the induction heating system used in this work for the production of the samples.

References

1. Special Metals, “Inconel 718 Properties,” n.d., p 28, <https://www.specialmetals.com/documents/technical-bulletins/inconel/inconel-alloy-718.pdf>. Accessed 28 July 2020
2. R.C. Reed, *The Superalloys: Fundamentals and Applications*, Cambridge University Press, Cambridge, 2006. <https://doi.org/10.1017/CBO9780511541285>
3. E. Akca and A. Gürsel, A Review on Superalloys and IN718 Nickel-Based INCONEL Superalloy, *PEN*, 2015 <https://doi.org/10.21533/pen.v3i1.43>
4. T.M. Pollock and S. Tin, Nickel-Based Superalloys for Advanced Turbine Engines: Chemistry, Microstructure and Properties, *J. Propuls. Power*, 2006, **22**(2), p 361-374.
5. C. Lyphout, P. Nylén and L. Östergren, Relationships Between Process Parameters, Microstructure, and Adhesion Strength of HVOF Sprayed IN718 Coatings, *J. Therm. Spray Tech.*, 2011, **20**(1-2), p 76-82.
6. C. Lyphout, P. Nylen and L.G. Östergren, Adhesion Strength of HVOF Sprayed IN718 Coatings, *J. Therm. Spray Tech.*, 2012, **21**(1), p 86-95.
7. C. Lyphout, A. Fasth and P. Nylen, Mechanical Property of HVOF Inconel 718 Coating for Aeronautic Repair, *J. Therm. Spray Tech.*, 2014, **23**(3), p 380-388.
8. C.S. Ramesh, D.S. Devaraj, R. Keshavamurthy and B.R. Sridhar, Slurry Erosive Wear Behaviour of Thermally Sprayed Inconel-718 Coatings by APS Process, *Wear*, 2011, **271**(9-10), p 1365-1371.
9. Z. Zhang, D.H.L. Seng, M. Lin, S.L. Teo, T.L. Meng, C.J.J. Lee, Z.-Q. Zhang, T. Ba, J. Guo, K. Sundaravivelu, P.K. Aw and J. Pan, Cold Spray Deposition of Inconel 718 in Comparison with Atmospheric Plasma Spray Deposition, *Appl. Surf. Sci.*, 2021, **535**, p 147704.
10. L.I. Pérez-Andrade, F. Gärtner, M. Villa-Vidaller, T. Klassen, J. Muñoz-Saldaña and J.M. Alvarado-Orozco, Optimization of Inconel 718 Thick Deposits by Cold Spray Processing and Annealing, *Surf. Coat. Technol.*, 2019, **378**, p 124997.
11. W. Sun, A.W.Y. Tan, A. Bhowmik, I. Marinescu, X. Song, W. Zhai, F. Li and E. Liu, Deposition Characteristics of Cold

- Sprayed Inconel 718 Particles on Inconel 718 Substrates with Different Surface Conditions, *Mater. Sci. Eng. A*, 2018, **720**, p 75–84.
12. W. Sun, A. Bhowmik, A.W.-Y. Tan, R. Li, F. Xue, I. Marinescu and E. Liu, Improving Microstructural and Mechanical Characteristics of Cold-Sprayed Inconel 718 Deposits via Local Induction Heat Treatment, *J. Alloys Compd.*, 2019, **797**, p 1268–1279.
 13. D. Levasseur, S. Yue and M. Brochu, Pressureless Sintering of Cold Sprayed Inconel 718 Deposit, *Mater. Sci. Eng. A*, 2012, **556**, p 343–350.
 14. W. Wong, E. Issou, P. Vo, M. Sone, F. Bernier, J.-G. Legoux, H. Fukunuma and S. Yue, Cold Spray Forming of Inconel 718, *J. Therm. Spray Tech.*, 2013, **22**(2–3), p 413–421.
 15. R. Singh, K.-H. Rauwald, E. Wessel, G. Mauer, S. Schrufer, A. Barth, S. Wilson and R. Vassen, Effects of Substrate Roughness and Spray-Angle on Deposition Behavior of Cold-Sprayed Inconel 718, *Surf. Coat. Technol.*, 2017, **319**, p 249–259.
 16. R. Singh, S. Schrufer, S. Wilson, J. Gibmeier and R. Vassen, Influence of Coating Thickness on Residual Stress and Adhesion-Strength of Cold-Sprayed Inconel 718 Coatings, *Surf. Coat. Technol.*, 2018, **350**, p 64–73.
 17. S. Bagherifard, G. Roscioli, M.V. Zuccoli, M. Hadi, G. D'Elia, A.G. Demir, B. Previtali, J. Kondás and M. Guagliano, Cold Spray Deposition of Freestanding Inconel Samples and Comparative Analysis with Selective Laser Melting, *J. Therm. Spray Tech.*, 2017, **26**(7), p 1517–1526.
 18. R. Vaßen, J. Fiebig, T. Kalfhaus, J. Gibmeier, A. Kostka and S. Schrüfer, Correlation of Microstructure and Properties of Cold Gas Sprayed INCONEL 718 Coatings, *J. Therm. Spray Tech.*, 2020 <https://doi.org/10.1007/s11666-020-00988-w>
 19. W. Ma, Y. Xie, C. Chen, H. Fukunuma, J. Wang, Z. Ren and R. Huang, Microstructural and Mechanical Properties of High-Performance Inconel 718 Alloy by Cold Spraying, *J. Alloys Compd.*, 2019, **792**, p 456–467.
 20. S.Y. Kim, V. Luzin, M.L. Sesso, J. Thornton and S. Gulizia, The Effect of Low Temperature Range Heat Treatment on the Residual Stress of Cold Gas Dynamic Sprayed Inconel 718 Coatings via Neutron Diffraction, *J. Therm. Spray Tech.*, 2020, **29**(6), p 1477–1497.
 21. L. Perez, J. Colburn, L. N. Brewer, M. Renfro, and T. McKechnie. (2021). Cold Spray Deposition of Heat-Treated Inconel 718 Powders. (Eds) by F. Azarmi, X. Chen, J. Cizek, C. Cojocar, B. Jodoin, H. Koivuluoto, Y. C. Lau, R. Fernandez, O. Ozdemir, H. Salimi Jazi, and F. Toma. (Virtual). doi:<https://doi.org/10.31399/asm.cp.itsc2021p0171>
 22. X.-T. Luo, M.-L. Yao, N. Ma, M. Takahashi and C.-J. Li, Deposition Behavior, Microstructure and Mechanical Properties of an in-Situ Micro-Forging Assisted Cold Spray Enabled Additively Manufactured Inconel 718 Alloy, *Mater. Des.*, 2018, **155**, p 384–395.
 23. M. Kazasidis, S. Yin, J. Cassidy, T. Volkov-Husović, M. Vlahović, S. Martinović, E. Kyriakopoulou and R. Lupoi, Microstructure and Cavitation Erosion Performance of Nickel-Inconel 718 Composite Coatings Produced with Cold Spray, *Surf. Coat. Technol.*, 2020, **382**, p 125195.
 24. W. Sun, A. Bhowmik, A.W.-Y. Tan, F. Xue, I. Marinescu, F. Li and E. Liu, Strategy of Incorporating Ni-Based Braze Alloy in Cold Sprayed Inconel 718 Coating, *Surf. Coat. Technol.*, 2019, **358**, p 1006–1012.
 25. W. Sun, A.W.-Y. Tan, D.J.Y. King, N.W. Khun, A. Bhowmik, I. Marinescu and E. Liu, Tribological Behavior of Cold Sprayed Inconel 718 Coatings at Room and Elevated Temperatures, *Surf. Coat. Technol.*, 2020, **385**, p 125386.
 26. G. Mauer, R. Singh, K.-H. Rauwald, S. Schrüfer, S. Wilson and R. Vaßen, Diagnostics of Cold-Sprayed Particle Velocities Approaching Critical Deposition Conditions, *J. Therm. Spray Tech.*, 2017, **26**(7), p 1423–1433.
 27. J. Villafuerte, *Modern Cold Spray: Materials, Process, and Applications*, Springer Verlag, Cham, 2015.
 28. H. Assadi, F. Gärtner, T. Stoltenhoff and H. Kreye, Bonding Mechanism in Cold Gas Spraying, *Acta Mater*, 2003, **51**(15), p 4379–4394.
 29. S. Rahmati and B. Jodoin, Physically Based Finite Element Modeling Method to Predict Metallic Bonding in Cold Spray, *J. Therm. Spray Tech.*, 2020, **29**(4), p 611–629.
 30. S. Rahmati, R.G.A. Veiga, A. Zúñiga and B. Jodoin, A Numerical Approach to Study the Oxide Layer Effect on Adhesion in Cold Spray, *J. Therm. Spray Tech.*, 2021 <https://doi.org/10.1007/s11666-021-01245-4>
 31. D.L. Gilmore, R.C. Dykhuizen, R.A. Neiser, T.J. Roemer and M.F. Smith, Particle Velocity and Deposition Efficiency in the Cold Spray Process, *J. Therm. Spray Tech.*, 1999, **8**(4), p 576–582.
 32. R.C. Dykhuizen and M.F. Smith, Gas Dynamic Principles of Cold Spray, *J. Therm. Spray Tech.*, 1998, **7**(2), p 205–212.
 33. S. Yin, X. Suo, H. Liao, Z. Guo and X. Wang, Significant Influence of Carrier Gas Temperature During the Cold Spray Process, *Surf. Eng.*, 2014, **30**(6), p 443–450.
 34. T. Schmidt, F. Gaertner and H. Kreye, New Developments in Cold Spray Based on Higher Gas and Particle Temperatures, *J. Therm. Spray Tech.*, 2006, **15**(4), p 488–494.
 35. A. Nastic, B. Jodoin, D. Poirier and J.-G. Legoux, Particle Temperature Effect in Cold Spray: A Study of Soft Particle Deposition on Hard Substrate, *Surf. Coat. Technol.*, 2021, **406**, p 126735.
 36. H. Assadi, T. Schmidt, H. Richter, J.-O. Kliemann, K. Binder, F. Gärtner, T. Klassen and H. Kreye, On Parameter Selection in Cold Spraying, *J. Therm. Spray Tech.*, 2011, **20**(6), p 1161–1176.
 37. T. Schmidt, F. Gärtner, H. Assadi and H. Kreye, Development of a Generalized Parameter Window for Cold Spray Deposition, *Acta Mater*, 2006, **54**(3), p 729–742.
 38. Y. Hao, J. Wang, X. Cui, J. Wu, T. Li and T. Xiong, Microstructure Characteristics and Mechanical Properties of Al-12Si Coatings on AZ31 Magnesium Alloy Produced by Cold Spray Technique, *J. Therm. Spray Tech.*, 2016, **25**(5), p 1020–1028.
 39. D.L. Guo, D. MacDonald, L. Zhao and B. Jodoin, Cold Spray MCrAlY Coatings on Single-Crystal Superalloy Using Nitrogen: Properties and Economics, *J. Therm. Spray Tech.*, 2020 <https://doi.org/10.1007/s11666-020-01058-x>
 40. R. Jenkins, S. Yin, B. Aldwell, M. Meyer and R. Lupoi, New Insights into the In-Process Densification Mechanism of Cold Spray Al Coatings: Low Deposition Efficiency Induced Densification, *J. Mater. Sci. Technol.*, 2019, **35**(3), p 427–431.
 41. M. Bray, A. Cockburn and W. O'Neill, The Laser-Assisted Cold Spray Process and Deposit Characterisation, *Surf. Coat. Technol.*, 2009, **203**(19), p 2851–2857.
 42. J. Yao, L. Yang, B. Li and Z. Li, Beneficial Effects of Laser Irradiation on the Deposition Process of Diamond/Ni60 Composite Coating with Cold Spray, *Appl. Surf. Sci.*, 2015, **330**, p 300–308.
 43. D.J. Barton, V.S. Bhattiprolu, G.B. Thompson and L.N. Brewer, Laser Assisted Cold Spray of AISI 4340 Steel, *Surf. Coat. Technol.*, 2020, **400**, p 126218.
 44. D.J. Barton, V.S. Bhattiprolu, B.C. Hornbuckle, C.M. Batali, K.A. Darling, G.B. Thompson and L.N. Brewer, Residual Stress Generation in Laser-Assisted Cold Spray Deposition of Oxide Dispersion Strengthened Fe91Ni8Zr1, *J. Therm. Spray Tech.*, 2020, **29**(6), p 1550–1563.
 45. D.J. Barton, B.C. Hornbuckle, K.A. Darling, L.N. Brewer and G.B. Thompson, Influence of Surface Temperature in the Laser Assisted Cold Spray Deposition of Sequential Oxide Dispersion

- Strengthened Layers: Microstructure and Hardness, *Mater. Sci. Eng. A*, 2021, **811**, p 141027.
46. R. Ortiz-Fernandez and B. Jodoin, Hybrid Additive Manufacturing Technology: Induction Heating Cold Spray—Part I: Fundamentals of Deposition Process, *J. Therm. Spray Tech.*, 2020, **29**(4), p 684–699.
 47. R. Ortiz-Fernandez and B. Jodoin, Hybrid Additive Manufacturing Technology: Induction Heating Cold Spray—Part II: Coating Mechanical Properties, *J. Therm. Spray Tech.*, 2020, **29**(4), p 700–713.
 48. M. Razavipour, J.-G. Legoux, D. Poirier, B. Guerreiro, J.D. Giallonardo and B. Jodoin, Artificial Neural Networks Approach for Hardness Prediction of Copper Cold Spray Laser Heat Treated Coatings, *J. Therm. Spray Tech.*, 2022, **31**(3), p 525–544.
 49. R. Ortiz-Fernandez, S. Imbriglio, R. Chromik and B. Jodoin, The Role of Substrate Preheating on the Adhesion Strength of Cold-Sprayed Soft Particles on Hard Substrates, *J. Therm. Spray Tech.*, 2021 <https://doi.org/10.1007/s11666-020-01148-w>
 50. F. Raletz, “Contribution Au Développement d’un Procédé de Projection Dynamique à Froid (P.D.F.) Pour La Réalisation de Dépôts de Nickel,” UNIVERSITÉ DE LIMOGES. (2005)
 51. D. MacDonald, S. Rahmati, B. Jodoin and W. Birtch, An Economical Approach to Cold Spray Using In-Line Nitrogen-Helium Blending, *J. Therm. Spray Tech.*, 2019, **28**(1–2), p 161–173.
 52. R. Lupoi and W. O’Neill, Powder Stream Characteristics in Cold Spray Nozzles, *Surf. Coat. Technol.*, 2011, **206**(6), p 1069–1076.
 53. B. Jodoin, Cold Spray Nozzle Mach Number Limitation, *J. Therm. Spray Tech.*, 2002, **11**(4), p 496–507.
 54. S. Yin, M. Meyer, W. Li, H. Liao and R. Lupoi, Gas Flow, Particle Acceleration, and Heat Transfer in Cold Spray: A Review, *J. Therm. Spray Tech.*, 2016, **25**(5), p 874–896.
 55. T. L. Bergman, A. Lavine, and F. P. Incropera, “Fundamentals of Heat and Mass Transfer.” (2017). <https://ebookcentral.proquest.com/lib/qut/detail.action?docID=5106220>. Accessed 20 September 2021
 56. Y.A. Çengel and M.A. Boles, *Thermodynamics: An Engineering Approach*, 7th ed. McGraw-Hill, New York, 2011.
 57. J. Braun, J. Sousa and G. Paniagua, Numerical Assessment of the Convective Heat Transfer in Rotating Detonation Combustors Using a Reduced-Order Model, *Appl. Sci.*, 2018, **8**(6), p 893.
 58. P. Liebersbach, A. Foelsche, V.K. Champagne, M. Siopis, A. Nardi and D.P. Schmidt, CFD Simulations of Feeder Tube Pressure Oscillations and Prediction of Clogging in Cold Spray Nozzles, *J. Therm. Spray Tech.*, 2020, **29**(3), p 400–412.
 59. H. Tabbara, S. Gu, D.G. McCartney, T.S. Price and P.H. Shipway, Study on Process Optimization of Cold Gas Spraying, *J. Therm. Spray Tech.*, 2011, **20**(3), p 608–620.
 60. S. Yin, Q. Liu, H. Liao and X. Wang, Effect of Injection Pressure on Particle Acceleration, Dispersion and Deposition in Cold Spray, *Comput. Mater. Sci.*, 2014, **90**, p 7–15.
 61. O.C. Ozdemir, C.A. Widener, D. Helfrich and F. Delfanian, Estimating the Effect of Helium and Nitrogen Mixing on Deposition Efficiency in Cold Spray, *J. Therm. Spray Tech.*, 2016, **25**(4), p 660–671.
 62. R. Huang and H. Fukunuma, Study of the Influence of Particle Velocity on Adhesive Strength of Cold Spray Deposits, *J. Therm. Spray Tech.*, 2012, **21**(3–4), p 541–549.
 63. X. Suo, S. Yin, M.-P. Planche, T. Liu and H. Liao, Strong Effect of Carrier Gas Species on Particle Velocity During Cold Spray Processes, *Surf. Coat. Technol.*, 2015, **268**, p 90–93.
 64. M. Faizan-Ur-Rab, S.H. Zahiri, S.H. Masood, M. Jahedi and R. Nagarajah, PIV Validation of 3D Multicomponent Model for Cold Spray Within Nitrogen and Helium Supersonic Flow Field, *J. Therm. Spray Tech.*, 2017, **26**(5), p 941–957.
 65. W. Wong, E. Irissou, A.N. Ryabinin, J.-G. Legoux and S. Yue, Influence of Helium and Nitrogen Gases on the Properties of Cold Gas Dynamic Sprayed Pure Titanium Coatings, *J. Therm. Spray Tech.*, 2011, **20**(1–2), p 213–226.
 66. A.G. McDonald, A.N. Ryabinin, E. Irissou and J.-G. Legoux, Gas-Substrate Heat Exchange During Cold-Gas Dynamic Spraying, *J. Therm. Spray Tech.*, 2013, **22**(2–3), p 391–397.
 67. J.G. Legoux, E. Irissou and C. Moreau, Effect of Substrate Temperature on the Formation Mechanism of Cold-Sprayed Aluminum, Zinc and Tin Coatings, *J. Therm. Spray Tech.*, 2007, **16**(5–6), p 619–626.
 68. A.N. Ryabinin, E. Irissou, A. McDonald and J.-G. Legoux, Simulation of Gas-Substrate Heat Exchange during Cold-Gas Dynamic Spraying, *Int. J. Therm. Sci.*, 2012, **56**, p 12–18.
 69. S.H. Zahiri, T.D. Phan, S.H. Masood and M. Jahedi, Development of Holistic Three-Dimensional Models for Cold Spray Supersonic Jet, *J. Therm. Spray Tech.*, 2014, **23**(6), p 919–933.
 70. D. MacDonald, R. Fernández, F. Delloro and B. Jodoin, Cold Spraying of Armstrong Process Titanium Powder for Additive Manufacturing, *J. Therm. Spray Tech.*, 2017, **26**(4), p 598–609.
 71. N. Fan, J. Cizek, C. Huang, X. Xie, Z. Chlup, R. Jenkins, R. Lupoi and S. Yin, A New Strategy for Strengthening Additively Manufactured Cold Spray Deposits through In-Process Densification, *Addit. Manuf.*, 2020, **36**, p 101626.
 72. S.V. Klinkov, V.F. Kosarev and M. Rein, Cold Spray Deposition: Significance of Particle Impact Phenomena, *Aerosp. Sci. Technol.*, 2005, **9**(7), p 582–591.
 73. A. Sova, S. Grigoriev, A. Kochetkova and I. Smurov, Influence of Powder Injection Point Position on Efficiency of Powder Preheating in Cold Spray: Numerical Study, *Surf. Coat. Technol.*, 2014, **242**, p 226–231.
 74. C.-J. Li, W.-Y. Li and H. Liao, Examination of the Critical Velocity for Deposition of Particles in Cold Spraying, *J. Therm. Spray Tech.*, 2006, **15**(2), p 212–222.
 75. L. Venkatesh, N.M. Chavan and G. Sundararajan, The Influence of Powder Particle Velocity and Microstructure on the Properties of Cold Sprayed Copper Coatings, *J. Therm. Spray Tech.*, 2011, **20**(5), p 1009–1021.
 76. X.-T. Luo, Y.-J. Li, C.-X. Li, G.-J. Yang and C.-J. Li, Effect of Spray Conditions on Deposition Behavior and Microstructure of Cold Sprayed Ni Coatings Sprayed with a Porous Electrolytic Ni Powder, *Surf. Coat. Technol.*, 2016, **289**, p 85–93.
 77. Q. Wang, N. Biribilis and M.-X. Zhang, Process Optimisation of Cold Spray Al Coating on AZ91 Alloy, *Surf. Eng.*, 2014, **30**(5), p 323–328.
 78. X. Meng, J. Zhang, J. Zhao, Y. Liang and Y. Zhang, Influence of Gas Temperature on Microstructure and Properties of Cold Spray 304SS Coating, *J. Mater. Sci. Technol.*, 2011, **27**(9), p 809–815.
 79. J. Ajaja, D. Goldbaum and R.R. Chromik, Characterization of Ti Cold Spray Coatings by Indentation Methods, *Acta Astronaut.*, 2011, **69**(11–12), p 923–928.
 80. P. Sudharshan Phani, D. Srinivasa Rao, S.V. Joshi and G. Sundararajan, Effect of Process Parameters and Heat Treatments on Properties of Cold Sprayed Copper Coatings, *J. Therm. Spray Tech.*, 2007, **16**(3), p 425–434.
 81. D. Goldbaum, J. Ajaja, R.R. Chromik, W. Wong, S. Yue, E. Irissou and J.-G. Legoux, Mechanical Behavior of Ti Cold Spray Coatings Determined by a Multi-Scale Indentation Method, *Mater. Sci. Eng. A*, 2011, **530**, p 253–265.
 82. W. Wong, P. Vo, E. Irissou, A.N. Ryabinin, J.-G. Legoux and S. Yue, Effect of Particle Morphology and Size Distribution on Cold-Sprayed Pure Titanium Coatings, *J. Therm. Spray Tech.*, 2013, **22**(7), p 1140–1153.
 83. G. Bae, Y. Xiong, S. Kumar, K. Kang and C. Lee, General Aspects of Interface Bonding in Kinetic Sprayed Coatings, *Acta Mater.*, 2008, **56**(17), p 4858–4868.

84. A. Fardan, C.C. Berndt and R. Ahmed, Numerical Modelling of Particle Impact and Residual Stresses in Cold Sprayed Coatings: A Review, *Surf. Coat. Technol.*, 2021, **409**, p 126835.
85. W. Li, K. Yang, D. Zhang and X. Zhou, Residual Stress Analysis of Cold-Sprayed Copper Coatings by Numerical Simulation, *J. Therm. Spray Tech.*, 2016, **25**(1–2), p 131–142.
86. A.S.M. Ang and C.C. Berndt, A Review of Testing Methods for Thermal Spray Coatings, *Int. Mater. Rev.*, 2014, **59**(4), p 179–223.
87. S. Kuroda and T.W. Clyne, The Quenching Stress in Thermally Sprayed Coatings, *Thin Solid Films*, 1991, **200**(1), p 49–66.
88. Y.-K. Wei, X.-T. Luo, Y. Ge, X. Chu, G.-S. Huang and C.-J. Li, Deposition of Fully Dense Al-Based Coatings via in-Situ Micro-Forging Assisted Cold Spray for Excellent Corrosion Protection of AZ31B Magnesium Alloy, *J. Alloys Compd.*, 2019, **806**, p 1116–1126.
89. R. Fernandez and B. Jodoin, Cold Spray Aluminum-Alumina Cermet Coatings: Effect of Alumina Content, *J. Therm. Spray Tech.*, 2018, **27**(4), p 603–623.
90. S.-L. Fu, C.-X. Li, Y.-K. Wei, X.-T. Luo, G.-J. Yang, C.-J. Li and J.-L. Li, Novel Method of Aluminum to Copper Bonding by Cold Spray, *J. Therm. Spray Tech.*, 2018, **27**(4), p 624–640.
91. Y. Xie, M.-P. Planche, R. Raelison, P. Hervé, X. Suo, P. He and H. Liao, Investigation on the Influence of Particle Preheating Temperature on Bonding of Cold-Sprayed Nickel Coatings, *Surf. Coat. Technol.*, 2017, **318**, p 99–105.

Publisher's Note Springer Nature remains neutral with regard to jurisdictional claims in published maps and institutional affiliations.

Springer Nature or its licensor (e.g. a society or other partner) holds exclusive rights to this article under a publishing agreement with the author(s) or other rightsholder(s); author self-archiving of the accepted manuscript version of this article is solely governed by the terms of such publishing agreement and applicable law.